ION WILEY

Development of the dual-frequency dual-constellation airborne multipath models

Mihaela-Simona Circiu[1,2] | **Stefano Caizzone[1]** | **Michael Felux[1]** |
Christoph Enneking[1] | **Markus Rippl[1]** | **Michael Meurer[1,2]**

[1]German Aerospace Center (DLR), Institute of Communications and Navigation, Wessling 82234, Germany

[2]RWTH Aachen University, Aachen, 52074, Germany

Correspondence
Mihaela-Simona Circiu, German Aerospace Center (DLR), Institute of Communications and Navigation, Wessling 82234, Germany.
Email: mihaela-simona.circiu@dlr.de

Funding information
European Commission, Grant/Award Number: 635/PP/GRO/RCH/17/9877

Abstract

This paper presents a methodology to build multipath models for aviation use of new Global Positioning System (GPS) and Galileo signals. The estimation of airframe multipath errors makes use of carrier phase measurements; thus, it is affected by the integer ambiguities. A new method for removing the ambiguities from the multipath estimation is presented. The method is suitable for measurements from flight data and is able to exclude measurements highly affected by multipath from the estimation by using a derived standard deviation based on the receiver thermal noise only. Next, an overview of the error sources relevant for the multipath estimation is given, and a first concept to separate the receiver antenna errors from the multipath errors is proposed. Finally, the paper discusses overbounding of the observed multipath errors to safely bound the tail risks and the inflation needed to account for uncertainty due to limited amounts of data.

1 | INTRODUCTION

The current Galileo constellation comprises 22 operational satellites, and more launches are planned in the coming years. All satellites broadcast signals in the E1 and E5a bands. Both bands are part of the aeronautical radio navigation service bands (ARNS) and thus are usable for aviation. From the GPS constellation, 12 satellites (Block IIF) are already broadcasting signals in the L1 and L5 bands, and all new satellites from Block III with their launch starting from this year (2019) will also include L5 signals. Therefore, the use of dual-frequency techniques becomes a promising solution for aviation users.

Before including new signals into the aviation application, it is necessary to assess their nominal performance with respect to noise and multipath. This evaluation is especially important because by using dual-frequency techniques, the previously dominant ionospheric error in single-frequency positioning is almost completely removed. Thus, the airborne multipath and noise errors gain a significantly more important role in the error budget. It is essential that the errors are well understood and assessed in order to be able to properly bound the residual errors and ensure integrity in GNSS-based applications, such as ARAIM and dual-frequency SBAS and GBAS.

In the current standards,[1,2] models using GPS L1 C/A code measurements were defined to characterize the airborne multipath and noise. One standard model has been developed for airborne multipath and noise error in order to avoid having different models and the associated difficulty in certification for each type of aircraft.[3-5] This model provides, however, an upper bound on the

expected multipath and noise error, and receiver manufacturers may use other models if the equipment shows better performance (below the defined curves). For future navigation service, aviation models for characterizing the single-frequency Galileo E1, Galileo E5a, and GPS L5 need to be developed. Furthermore, the availability of a second frequency enables the use of the ionospheric combination to eliminate dominant ionospheric errors. Thus, models characterizing multipath and noise errors in the ionospheric-free pseudoranges are also needed and will be discussed in this work.

To derive the airborne models, measurements from extensive flight trials were analyzed. Multipath errors were then estimated based on a code-minus-carrier method with ionospheric delay removal using dual-frequency carrier phase measurements (explained in Section 4). This estimation is not perfect as it is also affected by the ambiguities of the carrier phase measurements and antenna and receiver biases. Assuming no cycle slips have occurred in the carrier tracking loops, the carrier phase ambiguities are constant over a continuous satellite pass. In this work, we investigate and propose different steps to refine the multipath estimation that could be used in deriving future airborne multipath models.

Additional errors introduced by the receiver antenna on the code measurements (group delay variations) are also contained in the multipath estimation. Previous researches[6,7] have shown that these errors are not necessarily constant but depend on the frequency and angle of arrival of the signal. Furthermore, these errors can be very different for different antennas and will also vary with the installation of the antenna (eg, on a metallic structure). Until now, these errors were considered together with the multipath and noise error and bounded through the multipath model. This is not ideal because the obtained results would be very dependent on the antenna used and the derived models would be either very conservative (in case a low performance antenna is used) or optimistic (in case a good performing antenna is used) and not sufficiently bound the errors for all installations. In this work, the deterministic antenna errors will be eliminated from the multipath estimation results, thus showing for the first time a decomposition among antenna-related errors and multipath errors (ie, errors due to reflections from objects in the antenna far field).

2 | CURRENT AIRBORNE MULTIPATH MODELS

Aeronautical applications today use code measurements to estimate the position solution. In order to reduce high-frequency noise and multipath present in these measurements, carrier smoothing in the form of a Hatch filter is applied.[8] For the user application, the final metric of interest is therefore the multipath and code noise error distribution in the measurements after carrier smoothing.

In the current GPS L1 MOPS[1,2] airborne error model, the code tracking noise and multipath noise are parameterized as zero-mean Gaussian overbounds, and together, they form an error distribution expressed as a function of the elevation angle θ (relating to the horizon) of the satellite at hand:

$$\sigma^2_{air} = \sigma^2_{noise}(\theta) + \sigma^2_{mp}(\theta). \tag{1}$$

The reason for defining these error bounds relative to the horizon is that most of the time, commercial aircraft are flying straight and level and in this way, the attitude of the airframe (as a source of multipath reflections) does not need to be considered in the model making it easy to use.

The model describes the distribution of the airborne error for the 100-s smoothed measurements. The GPS L1 C/A standard models provide parameters for the noise and multipath functions for two performance classes of receiver/antenna combinations, Airborne Accuracy Designator A and B (AAD-A/AAD-B), where the multipath model is equal in both cases:

$$\sigma_{noise}(\theta) = \begin{cases} 0.15 + 0.43 \cdot \exp\left(-\dfrac{\theta}{6.9}\right) \text{ for AAD-A,} \\ 0.11 + 0.13 \cdot \exp\left(-\dfrac{\theta}{6.9}\right) \text{ for AAD-B,} \end{cases} \tag{2}$$

$$\sigma_{mp}(\theta) = 0.13 + 0.53 \cdot \exp\left(-\dfrac{\theta}{10}\right) \text{ for AAD-A and B.}$$

The current multipath error model was established based on measurements collected during hundreds of flight hours from different airframes.[3-5,9,10] The model is considered to bound both the multipath and antenna group delay variations for GPS L1 C/A code measurements.[10] Harris et al[10] show that the current receiver noise, multipath, and group delay variation error models are considered an adequate bound for GPS L1 errors in the position domain. This is because the current model bounds the errors in the range domain, while the overall goal for a safe operation is to bound the error in the position domain. Range domain is conservative in the sense that it assumes the worst combination of errors on all measurements.

3 | DATA COLLECTION FOR NEW MODELS

Since 2015, a Javad Delta TRE3 receiver and a multiband antenna have been permanently installed in DLR's Airbus A320 research aircraft in order to collect as much multi-frequency multi-constellation flight data as possible. Dual constellation (GPS and Galileo), dual-frequency (L1/E1-L5/E5a) measurements were collected by the onboard receiver at a rate of 20 Hz. The configuration of the receiver was chosen according to the current plans for standardization (ie, a 0.1 correlator chip spacing for L1/E1 and 1 chip for L5/E5a with a bandwidth of 23 MHz).[11] An avionics multiband antenna was installed on the aircraft, not in its primary location, but further back as marked by the arrow in the left image of Figure 1. The antenna used is not compliant with the recently published MOPS for dual-frequency airborne antennas.[12] It has a smaller axial ratio than the one required in the standards, and the group delay variations exceed the given limits. Thus, the results obtained from this experimental setup contain more noise and multipath than what is expected from compliant antennas and are therefore more conservative. The evaluations from this work are based on measurements from this setup. Data from 78 flights conducted between November 2015 and July 2017 are available, and a total of about 200 flight hours were collected and evaluated to derive the results from this work. Most of the flights took place in Europe with the exception of one transatlantic flight from Braunschweig to French Guyana and back.

In addition to the flight data, several ground tests were performed with a similar antenna and receiver to those installed on the aircraft. During the ground tests, the antenna was mounted on a rolled edges ground plane in order to approximate the installation on the aircraft as shown on the right in Figure 1 (details on the rolled edges ground plane are given in Caizzone et al[6]). The advantage of these static studies is that they can be performed over long time periods and allow collection of the measurements in a more controlled environment. These measurements will be used mainly for a detailed investigation of the antenna-induced errors and the validation of the calibration method.

4 | METHODOLOGY FOR MULTIPATH ESTIMATION

The multipath airborne models need to overbound the residual errors present in the code measurements after the carrier smoothing. Thus, the process of estimating the multipath should contain the same errors as in the smoothed measurements to the largest extent possible. This section describes the derivation of the multipath error models based on GNSS measurements. First, the methodology to estimate the raw multipath and noise error in the single-frequency and dual-frequency ionospheric-free (Ifree) combination is presented. Next, the steps applied to define the multipath models are discussed.

4.1 | Assessment of single-frequency multipath and noise error

A commonly used way to estimate the residual multipath and noise errors present in the single-frequency pseudorange measurements is to look at the code-minus-carrier (CMC) phase measurements. This approach assumes the carrier phase measurement to be ideal and unaffected by noise and multipath. While this is of course not entirely true, the carrier phase noise and carrier phase multipath errors are orders of magnitude smaller than the raw code multipath and noise errors. The ideal assumption is therefore suitable for the application of estimating airborne multipath. The equation for the code (pseudorange) and carrier phase measurements for a frequency i, receiver r, and satellite s is described by

$$\rho^s{}_{r,i} = R^s{}_{r,i} + c \cdot (\delta t_r - \delta t^s) + T^s_r + I^s_{r,i} + e^s_{r,i} + MP^s_{r,i} + \varepsilon^s_{r,i}$$
$$+ b^s_i + b_{r,i} + \xi_{r,i} + \xi^s_i,$$
$$\phi^s{}_{r,i} = R^s{}_{r,i} + c \cdot (\delta t_r - \delta t^s) \qquad (3)$$
$$+ T^s_r - I^s_{r,i} + e^s_{r,i} + N^s_{r,i} \cdot \lambda_i + mp^s_{r,i} + \eta^s_{r,i} + \beta^s_i + \beta_{r,i}$$
$$+ \zeta_{r,i} + \zeta^s_i,$$

FIGURE 1 Airbus A320 research aircraft "ATRA" used for the data collection. Location of the experimental GNSS antenna marked by the red arrow (left figure) and setup for ground tests (right figure) [Color figure can be viewed at wileyonlinelibrary.com and www.ion.org]

where $R^s_{r,i}$ is the geometric range from the receiver r to the satellite s (in m), c is the speed of light (in m/s), δt_r is the receiver clock bias (in s), δt^s is the satellite clock bias (in s), $I^s_{r,i}$ is the ionospheric delay for frequency i (in m), $T^s_{r,i}$ is the tropospheric delay (in m), $N^s_{r,i}$ and λ_i are the integer ambiguity (in cycles) and the corresponding wavelength of the frequency i, $MP^s_{r,i}, \varepsilon^s_{r,i}$ and $mp^s_{r,i}, \eta^s_{r,i}$ represent the multipath and thermal noise errors on the code and carrier phase measurements, respectively (in m), the $b^s_i, b_{r,i}$ represents the code-phase satellite and receiver instrumental errors (in m), and $\beta^s_i, \beta_{r,i}$ represents the carrier phase receiver and satellite instrumental errors (in m). The terms $\xi_{r,i}, \xi^s_i$ describe the errors introduced by the satellite and receiver antenna on code measurements on frequency i, and $\zeta_{r,i}, \zeta^s_i$ describe the satellite and receiver antenna errors introduced on the carrier phase measurements on frequency i. The equations are slightly modified from the usual form to include the additional receiver and transmitter instrumental and antenna biases. Differentiating the code and the carrier phase measurements leads to the CMC observable, which becomes

$$CMC^s_{r,i} = \rho^s_{r,i} - \phi^s_{r,i} = 2 \cdot I^s_{r,i} \tag{4}$$

$$+ \left(MP^s_{r,i} + \varepsilon^s_{r,i} + b^s_i + b_{r,i} + \xi_{r,i} + \xi^s_i \right)$$

$$- \left(N^s_{r,i} \cdot \lambda_i + mp^s_{r,i} + \eta^s_{r,i} + \beta^s_i + \beta_{r,i} + \zeta_{r,i} + \zeta^s_i \right).$$

The combination removes the clock errors, the tropospheric delay, and the ephemeris error. However, it contains twice the ionospheric delay, the carrier phase ambiguity, the combined code multipath and noise, the combined phase multipath and noise, and the code and carrier phase hardware delays (eg, instrumental delays and antenna errors). The ionospheric delay is frequency dependent, and the first-order relationship between the ionospheric delay experienced in the measurements (code and carrier phase) of two frequencies i and j is $I_j = f^2_i / f^2_j \cdot I_i$. Thus, the ionospheric delay between a satellite s and a receiver r on frequency i can be estimated by combining the dual-frequency carrier phase measurements as follows:

$$I^s_{r,i} = \frac{f^2_j}{f^2_i - f^2_j} \cdot \left(\phi^s_{r,i} - \phi^s_{r,j} \right) - \frac{f^2_j}{f^2_i - f^2_j}$$

$$\cdot \left(N^s_{r,i} \cdot \lambda_i - N^s_{r,j} \cdot \lambda_j \right) - \underbrace{\frac{f^2_j}{f^2_i - f^2_j} \cdot (E_i - E_j)}_{\approx 0}, \tag{5}$$

where the terms E_i and E_j replace the additional errors affecting the carrier phase measurements on frequency i

and j such as the carrier phase multipath and noise errors, carrier instrumental errors, and the carrier phase satellite and receiver antenna errors. Note again that these errors can be considered negligible as they are orders of magnitude smaller compared with the code noise and multipath error.

The carrier phase measurements are preferred for the estimation of the ionospheric delay because the noise and the multipath variance are some order of magnitudes lower compared with the code measurements. However, the estimated ionospheric delay is affected by the linear combination of the carrier phase ambiguities from the two frequencies. The carrier phase ambiguities, and thus their linear combinations, remain constant over a continuous tracking of the signal and are removed in the final bias removal step, which will be discussed in the next section.

By replacing the ionospheric delay estimation and subtracting twice the result from Equation (4), we obtain a biased estimate of the CMC with the ionospheric divergence removed. This observation is usually called CMC divergence free (noted as $CMC_{\text{Dfree,bias}}$ in this paper) and is expressed as follows:

$$CMC_{\text{Dfree,bias}}{}^s_{r,i} = CMC^s_{r,i} - 2 \cdot I^s_{r,i} = \rho^s_{r,i} - \phi^s_{r,i} \tag{6}$$

$$- \frac{2f^2_j}{f^2_i - f^2_j} \cdot \left(\phi^s_{r,i} - \phi^s_{r,j} \right).$$

Expanding the code and the carrier phase measurements using Equation (3), the $CMC_{\text{Dfree,bias}}{}^s_{r,i}$ can be written as follows:

$$CMC_{\text{Dfree,bias}}{}^s_{r,i} = \left(MP^s_{r,i} + \varepsilon^s_{r,i} + b^s_i + b_{r,i} + \xi_{r,i} + \xi^s_i \right)$$

$$- \left(mp^s_{r,i} + \eta^s_{r,i} + \beta^s_i + \beta_{r,i} + \zeta_{r,i} + \zeta^s_i \right) - \tag{7}$$

$$- \frac{2f^2_j}{f^2_i - f^2_j} \cdot \left(mp^s_{r,i,j} + \eta^s_{r,i,j} + \beta^s_{i,j} + \beta_{r,i,j} + \zeta_{r,i,j} + \zeta^s_{i,j} \right)$$

$$- N^s_{r,i} \cdot \lambda_i - \frac{2f^2_j}{f^2_i - f^2_j} \cdot \left(N^s_{r,i} \cdot \lambda_i - N^s_{r,j} \cdot \lambda_j \right).$$

The obtained $CMC_{\text{Dfree,bias}}$ contains the estimation of the single-frequency code noise and multipath. The estimates are biased by the carrier phase ambiguities and hardware biases. When using measurements from flight data, it becomes difficult to accurately estimate the carrier phase ambiguities through the ambiguities fixing algorithms (eg, lambda method) due to the aircraft movement and more frequent cycle slips and loss-of-lock events (compared with the static ground data). The frequent cycle slips can occur due to the fast change in the elevation and azimuth angles of the satellite and the

blockage of the signals during maneuvering. Furthermore, any error in the calculation of the ambiguities and hardware biases would project incorrectly into the multipath estimations. The typical approach is to consider that the carrier phase ambiguities and hardware biases are constant over a continuous pass of the satellite. This bias can then be removed as described in Section 5. We use the notation $CMC_{\text{Dfree}^s_{r,i}}$ for the estimates obtained after the ambiguities removal.

4.2 | Assessment of dual-frequency multipath and noise error

The availability of a second frequency enables the aviation user to form the ionospheric-free combinations and remove the dominant ionospheric error. The ionospheric-free combination of the code and phase measurements for L1/E1 and L5/E5a frequencies is formed as follows:

$$\rho_{\text{Ifree}_r^s} = \frac{f_1^2 \cdot \rho_{L1} - f_5^2 \cdot \rho_{L5}}{f_1^2 - f_5^2}, \phi_{\text{Ifree}_r^s} = \frac{f_1^2 \cdot \phi_{L1} - f_5^2 \cdot \phi_{L5}}{f_1^2 - f_5^2}. \quad (8)$$

The multipath present in the ionospheric-free pseudoranges can be estimated by forming the ionospheric-free combination on the single-frequency $CMC_{\text{Dfree}^s_{r,i}}$ (the estimate after the ambiguities removal):

$$CMC_{\text{Ifree}_r^s} = \frac{f_1^2 \cdot CMC_{\text{Dfree}_{r,L1}^s} - f_5^2 \cdot CMC_{\text{Dfree}_{r,L5}^s}}{f_1^2 - f_5^2}. \quad (9)$$

Another way to obtain an estimate of the ionospheric-free multipath and noise error is by differentiating the ionospheric-free combined code and carrier phase measurements. In this case, the observables are affected by the combination of the single-frequency ambiguities, and their removal is explained in the next section. However, the two methods lead to similar results.

4.3 | Definition of multipath models

The measurements-based multipath models as a function of elevation of the satellite are obtained from the raw multipath estimation (for single- or dual-frequency pseudoranges) following the steps described below:

- The CMC values are smoothed using the code-carrier smoothing (Hatch filter) as in the airborne processing. The code-carrier smoothing uses the rate of the precise carrier phase measurements to propagate code measurements forward. The carrier-smoothed code measurements are determined by averaging the pseudorange estimates over k epochs and reconstructing the smoothed pseudorange. The expression of the carrier smoothing was first introduced in Hatch[8] and was adopted further in the standards (see previous studies[1,2]). The smooth multipath at an epoch k is obtained by applying the same smoothing filter to the raw multipath and noise estimates (after carrier ambiguities removal). One of the implementations of the smoothing filter presented in the previous studies[1,2] is described as follows:

$$\overline{CMC_{\text{Dfree}^s_{r,i}}}(k) = \frac{\Delta t}{\tau} \cdot CMC_{\text{Dfree}^s_{r,i}}(k) + \left(1 - \frac{\Delta t}{\tau}\right) \quad (10)$$
$$\cdot \left[\overline{CMC_{\text{Dfree}^s_{r,i}}}(k-1)\right].$$

In this work, only the errors in the filter steady state (after the smoothing filter converged) are characterized. We consider that the filter reaches steady state after 3.6 times the smoothing time constant (eg, 360 seconds for 100-s smoothing time).[13] However, the receiver manufacturer can also implement a time variant version of this smoothing filter, in which case the measurements are used before the filter reaches steady state. The increase in the errors during the filter transient phase (from the filter initialization until the steady state) needs to be investigated and modeled in order to properly bound the errors, but this characterization is out of scope for this work.

- Computation of elevation angles
  Unlike atmospheric effects, multipath is a local effect, and airborne multipath is highly dependent on the airframe. Thus, the errors depend on the elevation and azimuth of the satellite relative to the aircraft. In our flight data evaluations, roll, pitch, and heading information from the basic aircraft instrumentation were used to translate the satellite coordinates into the aircraft body frame. The transformation from the coordinates in the ECEF to the coordinates in the body frame is performed as follows:
- First, the ECEF coordinates are transformed into local north-east-down (NED) coordinates using the relation:

$$\begin{bmatrix} x_{\text{NED}} \\ y_{\text{NED}} \\ z_{\text{NED}} \end{bmatrix} = \begin{bmatrix} -\sin\phi \cdot \cos\lambda & -\sin\phi \cdot \sin\lambda & \cos\phi \\ -\sin\lambda & \cos\lambda & 0 \\ -\cos\phi \cdot \cos\lambda & -\cos\phi \cdot \sin\lambda & -\sin\phi \end{bmatrix} \quad (11)$$
$$\cdot \begin{bmatrix} x_{\text{ECEF}} \\ y_{\text{ECEF}} \\ z_{\text{ECEF}} \end{bmatrix},$$

where ϕ and λ represent the latitude and longitude of the aircraft in WGS84 coordinates, respectively.

○ The NED coordinates are then transformed into the body frame coordinates by first performing a rotation by the third axis by the heading, then rotation around the second axis for the pitch, and finally by rotating the first axis by the roll as follows:

$$
\begin{bmatrix} x_{\text{BF}} \\ y_{\text{BF}} \\ z_{\text{BF}} \end{bmatrix} = \begin{bmatrix} \cos H & \sin H & 0 \\ -\sin H & \cos H & 0 \\ 0 & 0 & 1 \end{bmatrix} \cdot \begin{bmatrix} \cos P & 0 & -\sin P \\ 0 & 1 & 0 \\ \sin P & 0 & \cos P \end{bmatrix} \quad (12)
$$

$$
\cdot \begin{bmatrix} 1 & 0 & 0 \\ 0 & \cos R & \sin R \\ 0 & -\sin R & \cos R \end{bmatrix} \cdot \begin{bmatrix} x_{\text{NED}} \\ y_{\text{NED}} \\ z_{\text{NED}} \end{bmatrix},
$$

with H, P, and R being the heading angle (from the true north), pitch angle, and the roll angle, respectively. The body-fixed coordinate system refers to the nose right-wing down coordinate frame.

○ Finally, the elevation and azimuth angle in the body frame are obtained using the relation:

$$
El_{\text{BF}} = \arctan\left(\frac{-z_{\text{BF}}}{\sqrt{x^2_{\text{BF}} + y^2_{\text{BF}}}} \right); \quad (13)
$$

$$
Az_{\text{BF}} = \arctan\left(\frac{y_{\text{BF}}}{x_{\text{BF}}} \right),
$$

where $0°$ elevation angles denoted the horizon and the $90°$, the zenith. The azimuth angle is measured from $0°$ at the aircraft noise towards the right wing (which is $90°$).

• Statistics are generated by sorting data into elevation bins and computing the standard deviation of the multipath and noise for each bin.

Finally, the smooth estimates of the multipath and noise errors ($\overline{CMC_{\text{Dfree}}{}^s_{r,i}}$) that will be used to build the airborne multipath models are grouped into elevation bins according to the elevation of the satellites (in aircraft body frame or in the local-level frame). Section 11 provides a comparison of the models obtained in the two coordinate frames. The choice of the interval for independent samples is derived based on an analysis of the correlation of the multipath and noise errors discussed in Section 10.

In this work, models are proposed for the combination of the multipath and noise errors and are based on the smoothed code-minus-carrier data. While the multipath error is a function of the satellite angle of arrival in body frame, the receiver noise is a function of the C/No. The C/No depends mainly on two parameters: the transmitted power, which is a function of the satellite elevation angle above the horizon, and the gain pattern of the receiver antenna for which the angle of arrival in local body frame is relevant. Previous work presented a separation of the receiver noise error based on use of level flight data and a C/No model as a function of the satellite elevation.[4,5] A separation of noise and multipath was beyond the scope and will be addressed in future work. In this study, the models will describe the standard deviation of the smoothed code-minus-carrier data containing multipath and noise combined.

Evaluating only the RMS of the measurements may, however, not be conservative enough if the actual error distribution has heavier tails than the Gaussian distribution used to describe the data. Thus, in order to derive overbounding models, the tails of the distributions need to be taken into account. A cumulative distribution function (CDF) overbounding is then applied to inflate the final model. Furthermore, the multipath errors in one elevation bin may also have an azimuth dependency. This means that the multipath errors at a particular azimuth in the body frame may occur with higher probability than the tails of the bound for that elevation. This azimuth dependency can yield a nonzero mean for the distribution of the multipath error in an elevation bin. Such effects are also accommodated by the CDF overbounding method described in Section 9.

From a statistical point of view, the model should also account for the limited number of samples and the associated uncertainty in the estimated standard deviations of the errors in each elevation bin. This step will be described further in Section 10.

Summing up, the derived multipath models will be based on the estimated standard deviation of the smoothed code-minus-carrier data (sorted in elevation bins) and a method for bounding the tails and a subsequent accounting for the number of samples as proposed in Sections 9 and 10. The separation of the receiver noise is left for future work.

5 | REMOVAL OF THE CARRIER PHASE AMBIGUITIES

The carrier phase ambiguities are different for each satellite and change per satellite in case a cycle slip or loss of track occurs. This can happen due to banking during maneuvers or blockage of the signals by parts of the airframe (eg, the tail). Thus, the input to the ambiguities

removal algorithm is a continuous segment of the unsmoothed $CMC_{\text{Dfree,bias}}$ estimates for each satellite during which the receiver does not lose track of the signal and no cycle slips occur. An example of the separation of the $CMC_{\text{Dfree,bias}}$ in such segments for one satellite (PRN 8 from a flight conducted on May 12, 2016, around Magdeburg-Cochstedt Airport) is given in Figure 2 where the red lines indicate the presence of a cycle slip or the loss of lock.

The typical approach to estimate the ambiguities is to compute the mean over a segment of continuous tracking of each satellite. This approach assumes that the multipath has a Gaussian distribution with zero mean. In a low multipath scenario, this assumption holds, and the average over the full segment represents a good estimation of the carrier phase ambiguities. An example of such a data set is shown in Figure 3. One continuous segment of the $CMC_{\text{Dfree,bias}}$ for GPS L1 versus the elevation of a satellite is shown in the left plot (Figure 3A), and Figure 3B shows the histogram of this data set, and the yellow vertical line represents the estimated mean. The data were collected during a static ground scenario, in a low
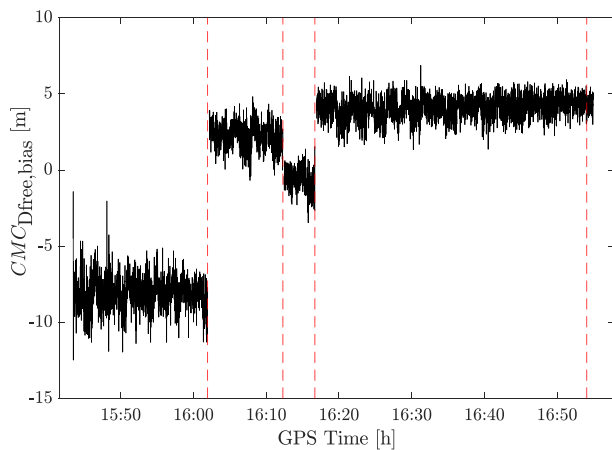
multipath environment (eg, not much multipath was expected at medium to high elevations). In this example, it can be observed that the multipath and noise error has an expected trend and decreases with the increase of the satellite elevation. The estimation of the carrier phase ambiguities of this segment can be done by calculating the mean; in this case, the mean of the noise and multipath errors can be assumed close to zero.

However, the measurements from flight tests show a different behavior. Figure 4 shows, in a similar manner as Figure 3, a continuous segment of the $CMC_{\text{Dfree,bias}}$ (during which no loss of track or cycle slip occurred) obtained from a flight test for one GPS satellite. The left graph shows the behavior versus elevation (Figure 4A), and the histogram of the data with its mean is shown in the right plot (Figure 4B). The elevation of the satellite refers to the elevation with respect to the aircraft body frame. The chosen flight contained long segments of straight and level, and thus, the satellite angles in the body frame show the difference to the elevation above horizon as small most of the time. In this case, we observe that the behavior of the multipath and noise errors as a function of elevation is different than in the previously shown ground case. The decrease of the multipath and noise error with the increase of elevation does not happen, and even measurements at higher elevations (between 60° and 80°) are strongly affected by multipath. The large multipath errors can lead to wrong estimation of the carrier phase ambiguities as the mean over the continuous segment.

Another approach to remove the carrier phase ambiguities is to subtract the bias at the position in the data set where the satellite elevation is the highest and the expected errors are the lowest. This method is again more suited for typical measurements from ground stations, where most of the multipath comes from low elevations. This assumption does not always hold for the measurements from flight tests. The multipath error on the aircraft is mainly created by the airframe, and thus, high

FIGURE 2 $CMC_{\text{Dfree,bias}}$ over time for one satellite [Color figure can be viewed at wileyonlinelibrary.com and www.ion.org]

FIGURE 3 $CMC_{\text{Dfree,bias}}$ versus elevation (A) and histogram of the $CMC_{\text{Dfree,bias}}$ (B) on GPS L1 for one satellite (PRN 10) [Color figure can be viewed at wileyonlinelibrary.com and www.ion.org]
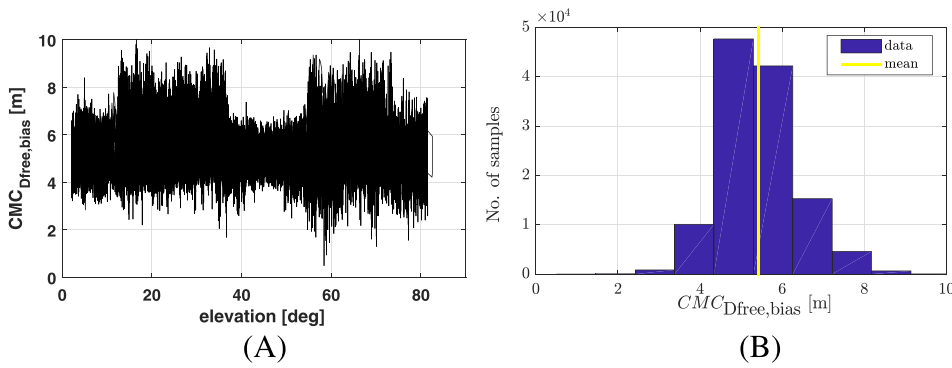
(A)   (B)
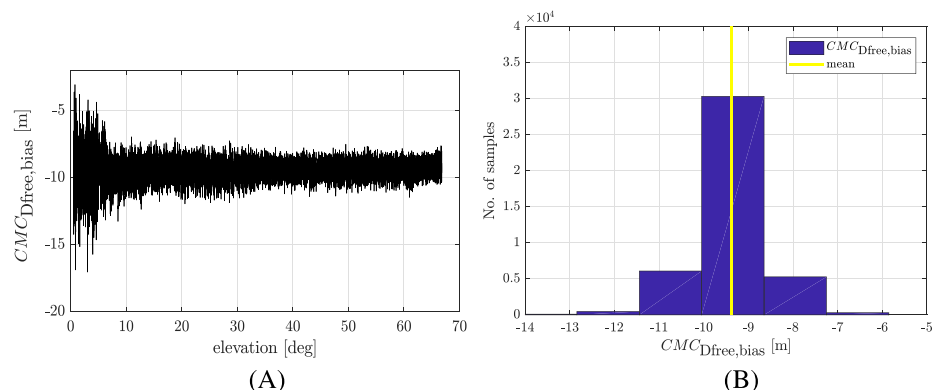
FIGURE 4 $CMC_{\text{Dfree,bias}}$ versus elevation (A) and histogram of the $CMC_{\text{Dfree,bias}}$ (B) on GPS L1 for one satellite (PRN 6) [Color figure can be viewed at wileyonlinelibrary.com and www.ion.org]

elevation satellites might also be affected by the reflections from the airframe components as observed in the case from Figure 4 (eg, measurements from elevations above 60° show an increased multipath error).

Thus, a new method is proposed. This method is intended to find portions from $CMC_{\text{Dfree,bias}}$ segments that are least affected by multipath and thus mainly contain receiver thermal noise. These clean portions of data are used to estimate the bias due to carrier phase ambiguities. The receiver thermal noise is zero mean Gaussian distributed and does not affect the estimation of the bias introduced by the carrier phase ambiguities and hardware errors.

1. The input to the algorithm is a continuous segment of the estimated $CMC_{\text{Dfree,bias}}$ (for one satellite).
2. Each data set ($CMC_{\text{Dfree,bias}}$ over one segment) is split into elevation bins (using the same binning used to compute the final models or fixed bins of, eg, 5°).
3. For each elevation bin, the standard deviation of the $CMC_{\text{Dfree,bias}}$ inside each bin is computed (noted here $\sigma_{CMC_{\text{Dfree,bias}}}$). This measured standard deviation is affected by the receiver thermal noise and multipath. The expected theoretical standard deviation due to the thermal noise (referred as σ_n^2) is computed using the theoretical reference model described by Kaplan and Hegarty[14]

$$\sigma_n = \sqrt{\frac{1}{T_C} \cdot \frac{B_L}{C/No} \cdot \frac{\int_{-B/2}^{B/2} S(f) \cdot \sin^2(\pi f \Delta) df}{\left(\int_{-B/2}^{B/2} 2 \cdot \pi \cdot f \cdot S(f) \cdot \sin(\pi f \Delta) df\right)^2} \cdot \left(1 + \frac{\int_{-B/2}^{B/2} S(f) \cdot \cos^2(\pi f \Delta) df}{\left(T \int_{-B/2}^{B/2} S(f) \cdot \cos(\pi f \Delta) df\right)^2}\right)}, \quad (14)$$

The expected receiver thermal noise (in terms of standard deviation) can be computed based on a theoretical model as a function of C/No as explained in more detail below. If the measurements do not contain large multipath errors, the standard deviation estimated from CMC values will be close to the theoretical standard deviation of the receiver noise only. Thus, the estimated standard deviation from the measurements is compared with the theoretically derived values. If both values agree reasonably well, the specific portion of data will be used in the computation of the carrier phase ambiguities. Otherwise, a large difference would hint at data being affected by other errors, which can affect the estimation of the carrier phase ambiguities. The steps of this method in more detail are described in the following:

with B_L being the one-sided bandwidth of the loop filter, B being the two-sided bandwidth of the receiver, Δ being the total correlator chip spacing (early minus late), T_C being the code period, C/No being the carrier-to-noise ratio, and T being the pre-detection integration time.

The power spectrum density for the binary phase shift keying (BPSK) signals used on GPS L1, GPS L5, and Galileo E5a is as follows:

$$S_{BPSK}(f) = T_C \cdot \left(\frac{\sin(\pi f T_C)}{\pi f T_C}\right)^2, \quad (15)$$

with T_c being 1/1.023 MHz for L1 and 1/10.23 MHz for the L5/E5a signals.

The Galileo E1 signal uses a CBOC(6,1,1/11) modulation with a dominant BOC(1,1) modulation

carrying 10/11 of the entire signal power. For aviation, only the BOC(1,1) component will be used, according to the current draft document of the dual-frequency standards.[11] Therefore, for the power spectrum density, the contribution of the BOC(1,1) component is considered, which is expressed as follows:

$$S_{BOC(1,1)}(f) = T_C \cdot \left(\frac{1 - \cos(\pi f T_C)}{\pi f T_C} \right)^2, \qquad (16)$$

with T_c being $1/1.023$ MHz.

The theoretical standard deviation computed based on Equation (14) gives an estimate of the standard deviation of $CMC_{\text{Dfree,bias}}$ in the presence of the thermal noise only, ie, without including the multipath. However, the calculation of the standard deviation of the receiver thermal noise only (σ_n) depends not directly on the elevation but is instead a function of the C/No values. The observed C/No values at each epoch cannot be used directly as they are affected by multipath, which changes the observed C/No values. Furthermore, the C/No is a function not only of the transmitted power of the satellite (and thus dependent on the elevation of the satellite above the horizon) but also of the gain pattern of the receiver antenna (and thus dependent on the angle of arrival in the aircraft body frame). Thus, a model for the C/No as a function of elevation in local-level frame is needed to estimate realistic values for the expected receiver thermal noise. In order to establish such a realistic model for the C/No function of elevation,

measurements from level flight portions from all flight tests available were combined. The level flight portions are used because the satellite angle of arrival in level frame coincides with the body frame angle. Figure 5 shows the distribution of the observed C/No values as a function of the satellite elevation angle in the airframe body frame for all signals with GPS L1 in Figure 5A, GPS L5 in Figure 5B, Galileo E1 in Figure 5C, and E5a in Figure 5D. The colors represent the number of samples (in logarithm scale) around that value, and the black curve shows the median over elevation bins. The median estimator was chosen to mitigate the effect of the large drops in the C/No values (which might be created by strong multipath).

4. Based on the expected standard deviation of the receiver thermal noise only, a one-sided hypothesis test with 5% false alarm for each elevation bin is formed following the two alternative hypotheses:

○ H_0: The data in the bin ($CMC_{\text{Dfree,bias}}$) are free of multipath, and the measurements are mainly affected by the receiver noise. If no large multipath is present in one elevation bin, we expect the standard deviation of the measured $CMC_{\text{Dfree,bias}}$ to be lower than the upper confidence limit of the thermal noise only (σ_n). In order to compute the upper confidence limit, we start from the statement that any estimate of a standard deviation based on a finite number of samples from a population has a chi-squared distribution with $n - 1$ degrees of freedom. Assuming that σ_n is the estimated standard

FIGURE 5 C/No values from level segments of flights for GPS L1 (left top plot), GPS L5 (right top plot), Galileo E1 (left bottom plot), and Galileo E5a (right bottom plot) [Color figure can be viewed at wileyonlinelibrary.com and www.ion.org]

(A) GPS L1 (B) GPS L5 (C) Galileo E1 (D) Galileo E5a
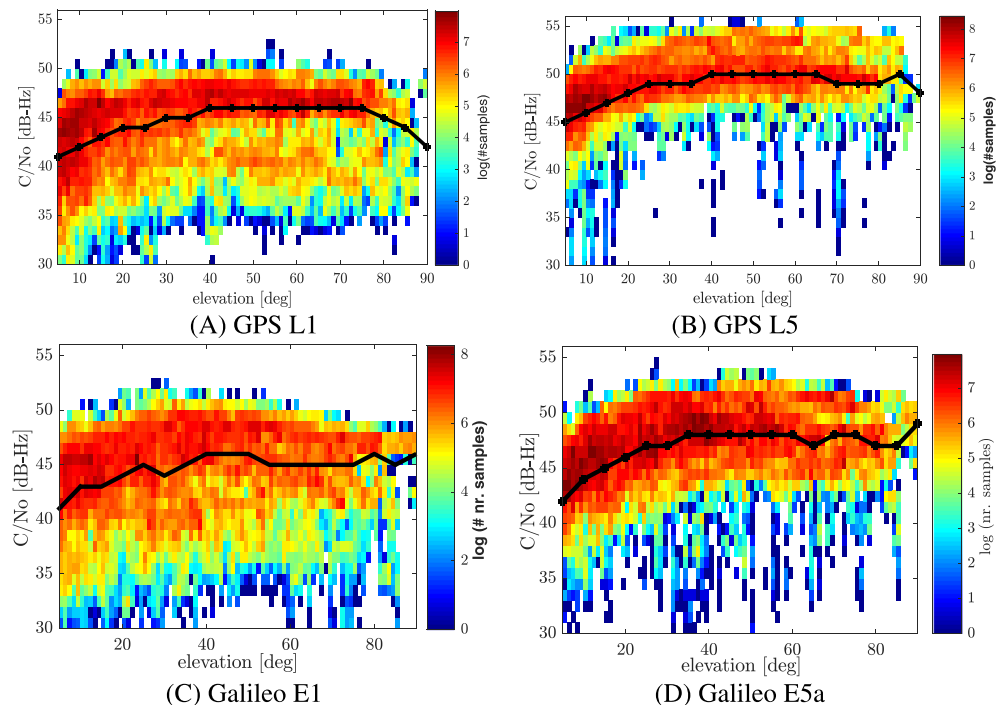
deviation, the upper confidence limit of the standard deviation is calculated as follows:

$$bound_{up} = \sigma_n \cdot \sqrt{\frac{n-1}{A}}, \qquad (17)$$

where A is the value for which χ^2_{n-1} has the probability $1 - \alpha$ (eg, for 95%, $\alpha = .05$) and n is the number of samples in the corresponding elevation bin. For this test, 95% upper bound is computed as it provides reasonably conservative bounds without inflating the expected standard deviation too large to allow high multipath to be accepted and without being too low to exclude all the measurements.

○ H_1: The data contain multipath or other errors and should not be considered in the computation of carrier phase ambiguities.

H_0 is accepted if the standard deviation of the
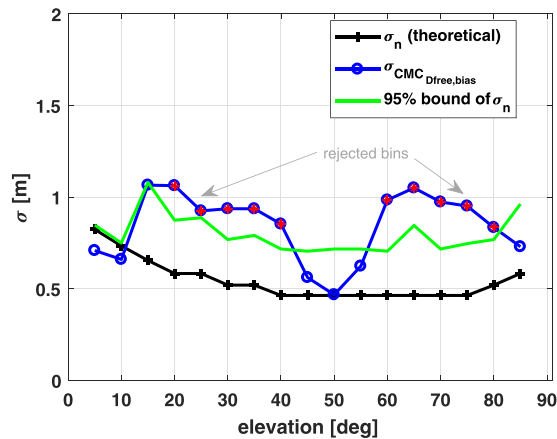
FIGURE 6 Improved method for bias removal. The plot shows the measured standard deviation of the $CMC_{\text{Dfree,bias}}$ (solid line with "o" marker), the expected theoretical standard deviation (solid line with "+" marker), and the upper bound of the hypothesis test (solid green line) [Color figure can be viewed at wileyonlinelibrary.com and www.ion.org]

$CMC_{\text{Dfree,bias}}$ ($\sigma_{CMC_{\text{Dfree,bias}}}$) is inside the defined confidence interval. If the value of the $\sigma_{CMC_{\text{Dfree,bias}}}$ is outside the defined region by the null hypothesis, it is rejected.

5. In the last step, the median over all the means of the accepted bins is computed as the estimation of the carrier phase ambiguities. The median is chosen because it is a more robust estimator to the outliers. The outliers in this case refer to the situation when one of the elevation bins has a low standard deviation, but its mean deviates from the general mean due to, eg, an undetected cycle slip.

Figure 6 shows an example of this method applied to the data set (the continuous segment of the $CMC_{\text{Dfree,bias}}$) of Figure 4. The black "+" curve represents the standard deviation due to noise only computed using Equation (14) (theoretical σ_n), and the upper bound of this standard deviation is represented with the green solid line. The variation of the upper bound is driven by the number of samples in each elevation bin. The blue curve (with "o" markers) shows the standard deviation computed from the measurements. It can be observed that the portions that are affected by large multipath (from 20° to 40° and 60° to 80°) exceed the acceptable bounds (green solid line) and thus are not considered in the calculation of the carrier phase ambiguities (the exclusion is shown with red "*" dots in the "o" markers). The first two values of the standard deviation computed from the measurements are below the theoretically derived curve and are not excluded by the algorithm. This behavior can be explained by larger C/No values experienced for those elevation angles compared with the median values that are used to compute the theoretical C/No model.

A comparison of the results obtained by the mean estimation and the improved method for the same data set (from Figure 4) is shown in Figure 7. The left plot represents the $CMC_{\text{Dfree,bias}}$ versus elevation, and the right plot represents the histogram of the data together with the value estimated as carrier phase ambiguity from the
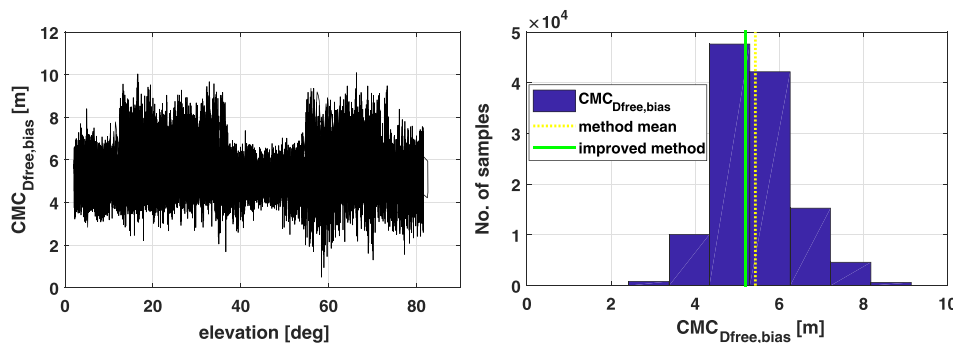

FIGURE 7 Comparison of different methods used for estimating the bias due to carrier phase ambiguities [Color figure can be viewed at wileyonlinelibrary.com and www.ion.org]

two methods: mean over the full segment (yellow dashed dot) and improved method (green line).

The difference between the values estimated by the two methods on the same set of data is up to 24 cm, which is significant in the multipath estimation context. If the entire data set is free of multipath, both methods should deliver very similar results. The improved method excludes portions of data from the given segment of $CMC_{\text{Dfree,bias}}$ values if the hypothesis of having multipath-free measurements is not supported. This approach ensures that the determination of the carrier phase ambiguities is less affected by external effects. The consequence of excluding this data is that we base our estimate on the measurements less affected by other errors. The exclusion of the measurements yields a larger uncertainty in the mean estimation, but the systematic error introduced in the estimation process of the carrier phase ambiguities is expected to be lower for the case when the segment for which the ambiguities are computed is affected by strong multipath errors that do not have a Gaussian distribution. Furthermore, the improved method is suitable for all phases of flight, not only for level flight. If during a maneuver, the elevation of the satellite changes significantly, those periods might exceed the theoretical bounds due to the increase in noise. This would however not affect the final estimation.

The examples are shown for the GPS L1 signal, but similar results have been obtained for all signals. The methodology can be applied also to the Ifree combination, where the theoretical noise corresponding to the combination is computed as follows:

$$\sigma_{n,\text{Ifree}} = \sqrt{\frac{f_1^4 \cdot \sigma^2_{n,L1} + f_5^4 \cdot \sigma^2_{n,L5}}{\left(f_1^2 - f_5^2\right)^2}}. \quad (18)$$

6 | ERRORS AFFECTING THE MULTIPATH ESTIMATION

The process of mean removal also eliminates any code and carrier phase biases that remain constant over a satellite pass such as the instrumental errors. However, additional errors introduced by the receiver and satellite antenna are also contained in the multipath estimates. Table 1 summarizes these biases from both satellite and receiver that are contained in the $CMC_{\text{Dfree,bias}}$.

6.1 | Errors not relevant for the multipath estimation

The satellite instrumental delay refers to the "delay between the signal radiated output of a specific SV (measured at the antenna phase center) and the output of that SV's onboard frequency source" (paragraph 3.3.17 of IS-GPS 200[15]). These delays are different for each frequency, each signal, and thus each satellite, and the final error present in the user measurements depends on the parameters used in the user receiver (eg, correlator spacing and receiver bandwidth). However, previous study[16] has shown that these biases are almost constant for each satellite and thus will not affect the multipath estimation being eliminated in the removal step.

In addition to the instrumental delays, the anisotropy of the satellite antenna introduces group delays on the code measurements and phase center variation on the carrier phase measurements. In recent years, it has been shown that these errors vary depending of nadir angle.[17] However, these errors are much smaller compared with the multipath error and the errors introduced by the receiver antenna. Thus, in this work, the contribution of

TABLE 1 Errors affecting the multipath estimation

Bias Type	Symbol	Variation With Time	Eliminated by Mean Removal
Code instrumental errors in the receiver	B_r	Constant over time the same for all satellites	Yes
Code instrumental errors in the satellite	B^s	Constant over time for each satellite	Yes
Phase instrumental errors in the receiver	β_r	Constant over time the same for all satellites	Yes
Phase instrumental errors in the satellite	β^s	Constant over time for each satellite	Yes
Code errors introduced by the receiver antenna	ξ_r	Varies with the angle of arrival	No
Code errors introduced by the satellite antenna	ξ^s	Varies function of the nadir angle	No
Phase errors introduced by the receiver antenna	ζ_r	Varies with the angle of arrival	No
Phase errors introduced by the satellite antenna	ζ^s	Small variations function of the nadir angle	No

the errors introduced by the satellite antenna is not considered further, and it is assumed that they are not dominant in the multipath estimation process.

The instrumental errors introduced by the user hardware processing chain (front-end, cables) are constant over time and are eliminated in the integer step removing the integer ambiguities. These errors are common to all satellites and will not affect the position solution because they will project into the receiver clock estimation.

6.2 | Errors relevant for the multipath estimation

In addition to the instrumental errors, the receiver antenna introduces errors on both code and phase measurements. Unlike the errors introduced by the satellite antenna, these errors can be much larger and need to be considered. Caizzone et al[7] have shown that the receiver antenna impacts the GNSS measurements via the differential group delay, the phase center variation, the gain, and the cross-polarization isolation. The gain and the cross polarization isolation have a direct impact into the amount of multipath that is present in the GNSS measurements. The differential group delay is defined as "time-delay difference that each frequency component of the signal experiences while passing through the antenna."[7] This parameter affects the code measurements and varies with the frequency as well as with the azimuth and elevation of the satellite. A detailed explanation of the derivation of the group delay variation and its relation with the antenna gain and phase pattern is given in Caizzone et al.[6,7] The second effect, the phase center variation, has an impact on the carrier phase measurements by "erroneously adding a phase contribution (variable with satellite elevation and azimuth) not due to the actual distance from the satellite, but to the antenna characteristics."[7] While the errors introduced by the phase center variation are rather small and are only of interest for high-precision application, the errors introduced on the code measurements can reach meter level. Thus, these errors will affect the multipath estimation, need to be taken into account, and are discussed in the next section.

7 | CODE ERRORS INTRODUCED BY THE RECEIVER ANTENNA

The differential group delay is directly impacted by the pattern uniformity of the antenna, meaning that if the pattern of the antenna is isotropic within the frequency band(s) of interest, the group delay will be equal for all elevation and azimuth angles and will project only into the receiver clock estimation.

The antenna-related errors ξ_r induced in the code measurements can be deterministically estimated by measuring the antenna phase patterns for each frequency in an anechoic chamber. The imperfection of the antenna response will propagate through the receiver and will result in code tracking biases. These biases depend on the GNSS signal that is being used. In order to estimate the code errors due to the group delay variations, the antenna response function is passed through an ideal receiver. Using the antenna and phase response versus frequency, the methodology described in Vergara et al[18] for analog distortions is used to calculate the code tracking error biases. The method considered jointly all the frequencies within the GNSS signal bandwidth. The work of Caizzone et al[7] discussed in more detail the derivation of the antenna introduced errors and presented an experimental validation of the estimated errors using GNSS measurements from a low multipath environment. The results showed that the estimation of the code error biases is very similar to the actual errors obtained from the measurements. Thus, in this paper, the code error estimated from the ideal receiver is further considered. An approximation of the installed performance of an antenna on the aircraft (which modifies the antenna radiation pattern) is obtained by measuring the antennas when mounted on a rolled edges ground plane.

Figure 8 shows the code errors due to the absolute antenna group delays for GPS L1 C/A code with BPSK(1) modulation (Figure 8A), for Galileo E1 (Figure 8B) for which a BOC(1,1) replica was used, and for GPS L5/Galileo E5a with the BPSK(10) modulation (Figure 8C) for all azimuth and elevation angles for the antenna mounted on DLR′s A320.
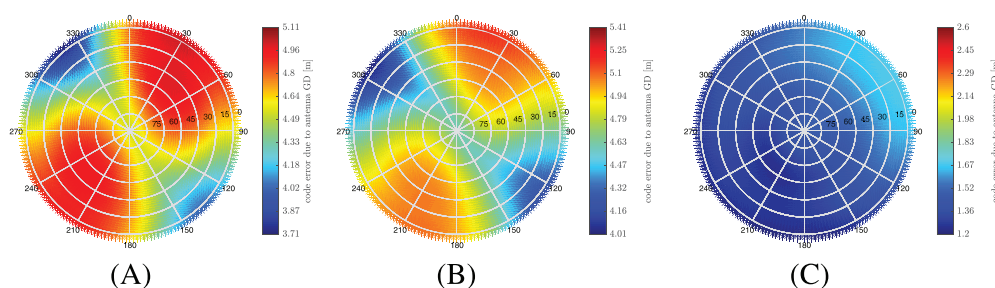

(A) (B) (C)

FIGURE 8 Code error due to the absolute antenna group delay for GPS L1 signal (A), Galileo E1 (B), and GPS L5/Galileo E5a (C) [Color figure can be viewed at wileyonlinelibrary.com and www.ion.org]

The absolute group delay refers to the total amount of error introduced by the antenna comprising also the effect of the active components of the antenna, which are common to all satellites and will project into the receiver clock estimation if not corrected. Thus, the absolute ranges for the three signals are different, and therefore, the scale in the two graphs is chosen accordingly. However, the total variation of 1.4 m among the entire hemisphere is kept identical. Looking at these figures, we can conclude that the code errors due to the antenna group delay are different for each frequency and show large variations over the angle of arrival (in this case, up to 1.4 m for L1 and 0.5 m for L5). A significant spatial variation is observed at L1 and E1, and the variation at L5 is smaller but still relevant. For Galileo E5a, the results are the same as for L5, since both use a BPSK(10) modulation.

In order to understand how these errors behave and affect the user in real time, we analyzed them in three different scenarios. The results for GPS L1 in terms of code errors versus time are shown in Figure 9. The three scenarios considered are as follows:

- A ground static scenario in which the antenna was mounted in the field in the DLR campus in Oberpfaffenhofen for approximatively 12 hours (Figure 9A)
- Level flight segment of around 1 hour (during which no turn and no change of heading occurred) from a flight test (Figure 9B)
- Segments with maneuvers from flight tests (Figure 9C)

For each scenario, the code errors shown in Figure 9 are computed from the actual geometry and taking the corresponding values derived for the L1 BPSK(1) signal for the specific angle (Figure 8A for the entire hemisphere). This means that the values are based not on GNSS measurements but on the estimations computed using an ideal receiver (with the configuration of the bandwidth and correlator spacing matching the Javad receiver) from the antenna frequency response. Note that during the flight tests, the elevation and azimuth refer to the angles in aircraft body frame.

In the first static test (Figure 9A), we observe that the variation of the antenna errors introduced by the group delay is changing slowly only due to the movement of the satellites and looks more bias like and is very different for each satellite. A similar behavior can be observed during a level flight (Figure 9B), during which the variation of the errors is again caused only by the movement of the satellite. However, this behavior changes completely during the maneuvers, and the variation is much larger due to the fast change in the satellite angle with respect to the antenna. This can be observed in the third plot (Figure 9C) where the geometry from a flight with approximatively 30 approaches around Braunschweig airport was considered. The bias-like behavior in the errors is only present over a short time (eg, 5-10 minutes) for the period of one maneuver.

These variations can lead to large position errors. Especially when considering the variation on both frequencies for a combination of the signals into an Ifree
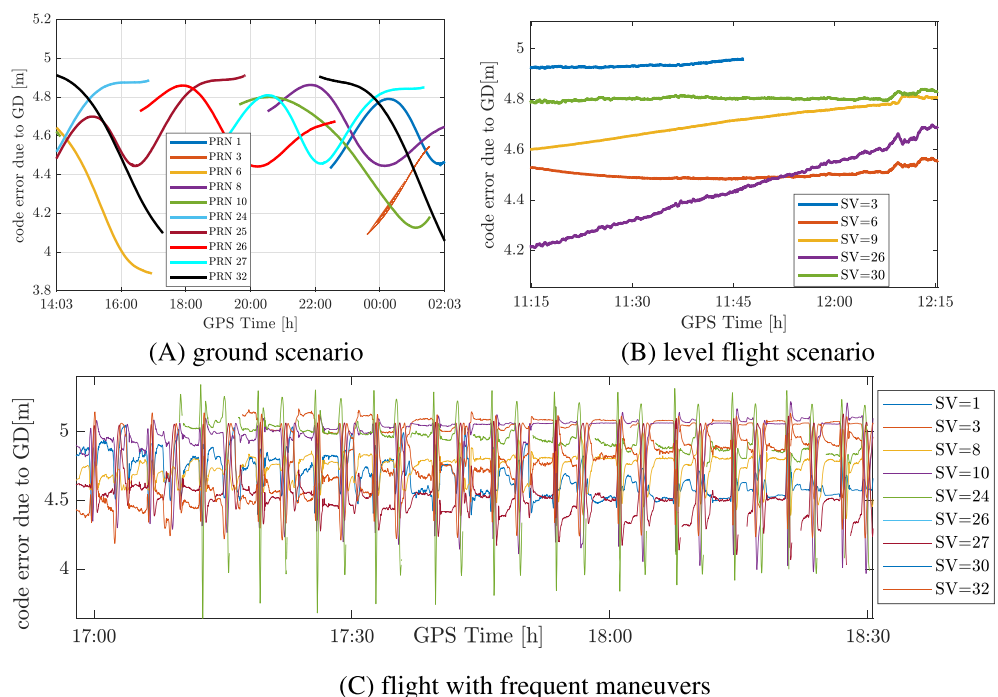

FIGURE 9 Estimated code error due to antenna group delay for different scenarios [Color figure can be viewed at wileyonlinelibrary.com and www.ion.org]

(A) ground scenario

(B) level flight scenario

(C) flight with frequent maneuvers

position solution, these errors become quite significant. In order to assess the actual position errors, a study for the static scenario shown in Figure 9A was performed. At each epoch, using the actual geometry, the code errors were estimated from the results over the whole hemisphere presented in Figure 8. The process is the same as the one used to derive the results in the graphs of Figure 9. The code errors for both frequencies L1 and L5 were calculated to derive the errors present in the Ifree combination. These code errors were then projected into the position solution. Figure 10 shows a plot of the 3-D position errors introduced by the antenna biases only. Note that these errors are specific to the geometry observed from Oberpfaffenhofen during the chosen period (1 hour and 40 minutes). The black curve shows the effect for single-frequency L1 positioning, while the red dashed curve shows the variations when forming the Ifree combination. The part common to all satellites from the absolute group delay projects into the receiver clock estimation, but the variations in the position error are due to the variation of the errors.

According to the current MOPS for aviation based on GPS L1 only,[1,2] the errors introduced by the antenna group delay were bounded together with the multipath errors. However, the previous results show that the behavior of these errors is quite different from the multipath errors, which are noise-like considered to be zero mean and are characterized by a standard deviation value. These errors are more bias like during a level flight segment showing a strong correlation over time. Faster variations occur during maneuvering due to the fast changing angle of arrival of the signal. Furthermore, the integer ambiguities removal will eliminate part of these errors. Consequently, it cannot be guaranteed that the
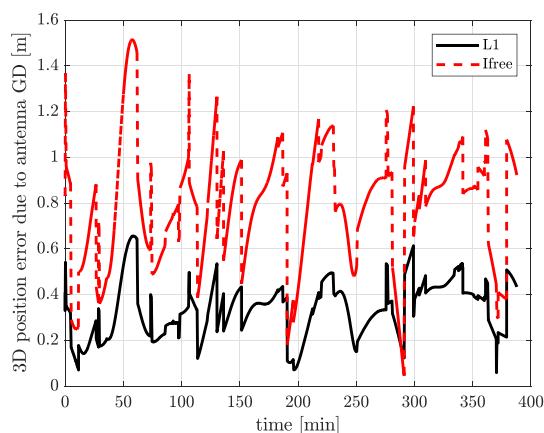
bound is always conservative and covers all cases. The errors present at the user are very dependent on the flight type (eg, level flight and maneuvers), and the bound should consider the worst case in order to ensure integrity. As a consequence, in this paper, we propose a separation of these errors from the multipath estimation, and the methodology is discussed in the next section.

8 | SEPARATION OF MULTIPATH ERROR AND ANTENNA-INDUCED ERROR

In order to ensure that the total error introduced by the antenna is eliminated from the multipath estimation, the calibration of the antenna-induced errors is applied before the integer ambiguities removal (on $CMC_{\text{Dfree,bias}}$ estimates). This is necessary because otherwise, the integer ambiguity removal would also remove parts of the antenna-introduced errors. The absolute code errors introduced by the antenna are computed for each satellite taking the actual elevation and azimuth of the satellite and using the corresponding values from Figure 8 as explained in the previous section. For measurements from flight tests, it is important to mention that the elevation and the azimuth angles are computed with respect to the body frame as the antenna-induced error depends on the arrival angle to the antenna.

Figure 11 shows the effect of the antenna calibration on the smooth multipath and noise error (CMC_{Dfree}) for GPS L1 for one satellite (left plot) together with the estimated code error group delay versus time (right plot). The black curve in the left plot shows the smooth error versus time before the calibration, and the green dashed curve represents the errors obtained after the antenna-induced errors are removed. The calibration removes the drift from the multipath error, and the resulting curve shows a much smoother behavior, which is expected for the multipath error. In a similar manner, Figure 12 shows the effect of the calibration during flight tests. In this case, the antenna-induced error (right plot) shows a larger variation due to the fast change in the angles of arrival during maneuvering. The calibration of the antenna errors also reduces the variation of the smooth multipath error (dashed green curve in the left plot) in this case significantly.

These results show that by removing the code errors due to antenna imperfection, we are able to extract the trend of the antenna errors from the multipath estimation. These errors constitute the near-field errors due to the antenna pattern. The remaining errors are due to the reflections from the antenna far field, namely, reflectors. The amount of multipath created by the far field

FIGURE 10 Position errors due to antenna biases for single-frequency positioning (black curve) and dual-frequency Ifree positioning (dashed red curve) [Color figure can be viewed at wileyonlinelibrary.com and www.ion.org]

FIGURE 11 Calibration of antenna errors in a static ground scenario. The left plot shows the smooth multipath and noise on GPS L1 for one satellite before calibration (black solid curve) and after calibration (dashed green curve). The right plot shows the code error due to antenna group delay variation [Color figure can be viewed at wileyonlinelibrary.com and www.ion.org]
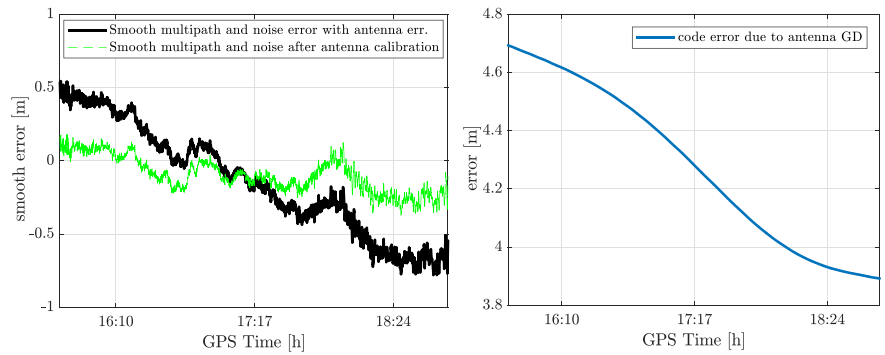

FIGURE 12 Calibration of antenna errors on measurements from flight. The left plot shows the smooth multipath and noise on GPS L1 for one satellite before calibration (black solid curve) and after calibration (dashed green curve). The right plot shows the code error due to antenna group delay variation [Color figure can be viewed at wileyonlinelibrary.com and www.ion.org]
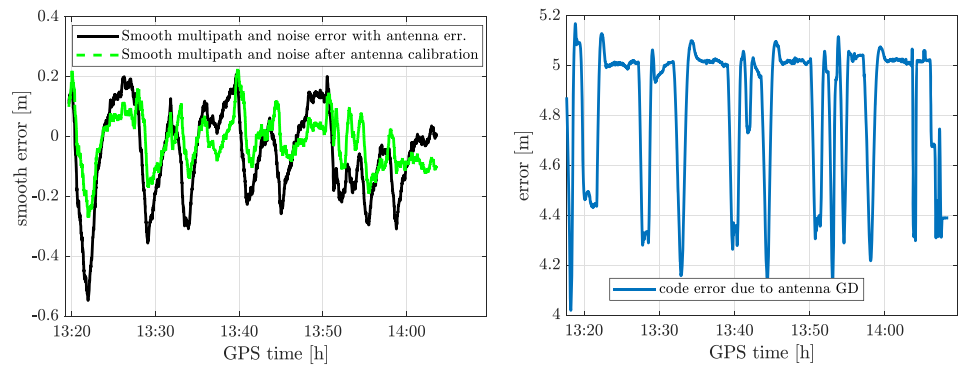
reflectors and present in the code measurements is dependent on the specific antenna rejection capabilities. Vergara et al[18] provide an analysis from the antenna point of view and discuss the parameters relevant for the multipath susceptibility. It should be noted however that when removing the errors introduced by the antenna group delay variations from the multipath error budget, they need to be accounted for separately in the integrity concept. This analysis is out of the scope of this paper, and future work will investigate the bounding of the antenna-induced errors.

9 | OVERBOUNDING OF THE TAILS

Typically, the smooth multipath and noise error in each elevation bin is modeled as a Gaussian distribution with zero mean and the standard deviation derived from the measurements. This statement cannot always be assumed for the true error distribution. In order to avoid underestimating the probability of errors larger than the Gaussian model, an overbounding Gaussian distribution is used to model the data. The CDF overbounding is defined as follows:

$$\Phi_{overbound}(x) \geq \Phi(x) \text{ for all } x \leq x - \sigma_{Gaussian fit}$$
$$\Phi_{overbound}(x) \leq \Phi(x) \text{ for all } x \geq x - \sigma_{Gaussian fit}, \quad (19)$$

with $\Phi(x) = \int_{-\infty}^{x} f(x)dx$ being the CDF of the random variable x with a Gaussian probability function. As the integral of the probability density function is always 1, the overbounding condition is not fulfilled for all data points but can be defined for examples to hold outside $\pm 1\sigma$ of the Gaussian fit.

Figure 13 shows an example of the overbounding for one elevation bin (14°-16° in this case) for Galileo E1 smooth multipath data. The black solid lines represent the cumulative distribution function (CDF) and 1-CDF of the smooth multipath error measured in the specific elevation bin, the blue dashed line represents the Gaussian fit, and the green dot line represents the overbound. It can be observed that in the range of roughly ±0.5 m, the Gaussian fits quite well in accordance with the sample data. However, for larger errors, the Gaussian fit model underestimates the probability of occurrence by orders of magnitude. As the multipath model is used for integrity purposes, this behavior should be prevented by using an overbound.

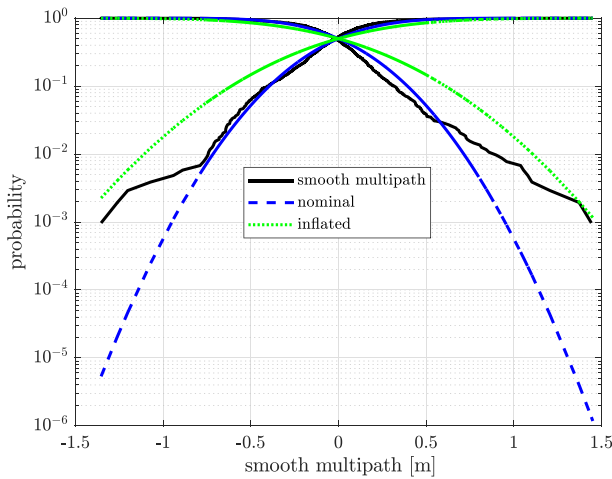This overbounding is more conservative than using a fit but ensures that the model conservatively bounds the

FIGURE 13 Example of overbounding for one elevation bin. The black curve shows the smooth multipath in the bin, the blue dashed curve shows the Gaussian fit, and the green dot curve shows the Gaussian overbound [Color figure can be viewed at wileyonlinelibrary.com and www.ion.org]

observed multipath errors. The inflation factors for the overbounding sigmas are derived independently for each single-frequency and dual-frequency models. It is important to note that when separating the measurements into elevation bins, the overbounding is applied over all azimuth angles from a specific elevation bin. This means that for a specific azimuth, the bound may not provide the same bounding probability as another azimuth as multipath originates from certain parts of the aircraft (eg, the tail fin). However, in order to build multipath models, a significant number of samples are required in order to ensure that the elevation and azimuth variation are well represented in the data.

This overbounding is not sufficient to ensure bounding of position errors with the required integrity risk and is only applied in the derivation of the multipath error models. The overbounding concept, while not stable through the convolution of errors, is generally considered to be sufficient for integrity purposes within the multipath models.

10 | INFLATION FOR THE LIMITED NUMBER OF SAMPLES

The values derived from the measurements are based on a limited number of samples, and thus, the measured standard deviation is not directly the true standard deviation of the data. In order to ensure statistical representability of the data, a further inflation factor is applied to the values derived from the limited amount of data. The inflation of the measurements-based standard deviations

with respect to the true is determined based on the chi-squared distribution of the standard deviation as follows:

$$\text{inflation} = \sqrt{\frac{n-1}{A}}, \qquad (20)$$

with n as the effective number of independent samples used to derive the standard deviation in each elevation bin and A as the value for which the chi-square distribution χ^2_{n-1} has the probability $1 - \alpha$ (for 95%, $\alpha = .05$). The reason for choosing this formula is because the variance estimate from a finite number of samples is a random variable with a chi-squared distribution with $(n - 1)$ degrees of freedom. The 95% confidence bound is chosen in this work as a parameter that provides reasonably conservative bounds without inflating the model too far to impact the availability (also suggested in the work of validating the existing airborne GPS L1 models as described in Booth et al[3]). However, the final result is not very sensitive to the confidence bound because if enough samples are collected, the difference in the inflation factor between different confidence bounds is rather small.

The driving factor in the derivation of the inflation factor is the number of independent samples in each elevation bin. In order to derive the effective number of the independent samples, the correlation of the multipath error needs to be taken into account. Even if the antenna-induced errors are removed (which would create stronger correlation over time), the multipath error might still be correlated especially during level flights where the geometry of the satellite changes slowly and multipath effects are somewhat static. As the final multipath curves are derived based on the 100-s smoothed multipath and noise errors, the correlation of the errors after smoothing needs to be taken into account. Figure 14 shows the median of the autocorrelation function using measurements from all available flight tests. The black solid curves show the autocorrelation of the raw (unsmoothed) multipath and noise error, and the blue dashed curve shows the autocorrelation of the 100-s smoothed multipath error. The 0.2 threshold is assumed as the limit for weak correlation (typically considered in statistics). It can be observed that the raw multipath error does not show strong correlation even for lags below 50 seconds. However, the smoothed multipath error is highly correlated for lags lower than 300 seconds, and it reaches the 0.2 threshold only after 350 seconds. Based on this result, we choose (preliminary) independent samples after 350 seconds.

Another factor that derives the inflation for the number of samples is the size of the selected elevation bins. In the derivation of ground multipath models (described in Eurocae ED-114A[13]), variable bin sizes are considered to
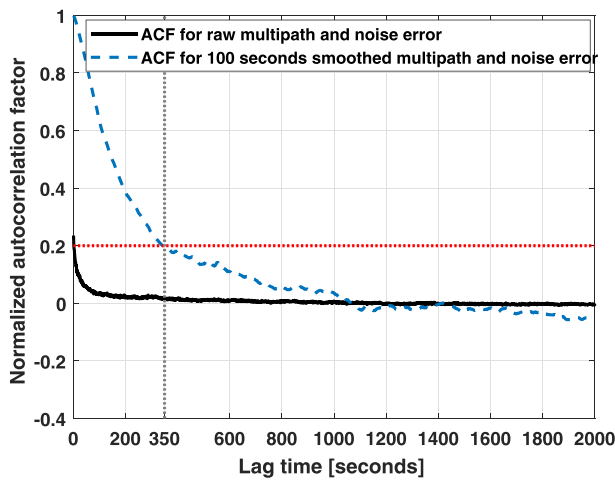
FIGURE 14 Median autocorrelation function of raw multipath error (black solid curve) and 100-second smoothed multipath (blue dashed curve) [Color figure can be viewed at wileyonlinelibrary.com and www.ion.org]

account for the different movement of the satellite for different elevations (fast at low elevation and slower at higher elevations) and also because it is assumed that higher elevations always have lower errors. However, this is not always the case for the airborne measurements in which, due to maneuvers, the satellite directions might change fast.

One approach would thus be to consider equal bin size (eg, a size of 2°) over all elevations. The resulting inflation factor together with the number of samples per elevation bin obtained for GPS is shown in Figure 15.

The results are derived based on the data collected from DLR flight tests (around 200 hours of flights). It can be observed that the inflation factor is rather constant except for the high elevation (above 80°), where the number of samples decreased significantly yielding an increased inflation factor. This increase might affect the final models and their elevation dependency. This is because it cannot be assumed that airborne multipath error is smaller for higher elevations, as the multipath received depends on the specific airframe geometry (eg, the tail can create multipath on high elevation satellites). A second approach to define the binning is by selecting bins with equal number of samples. An example of such binning is shown in Figure 16 together with the inflation factor. In this case, the inflation factor is constant over elevation, but the drawback of this approach is that the width of the bins is larger for high elevation and thus could introduce unacceptable average. However, the decision of the elevation bins for the final model must be made based on the specific data set and the trade-off between the increase in the inflation factor and the averaging. For our data set, the inflation based on the bins with equal number of samples will be used.

11 | PRELIMINARY MULTIPATH MODELS

This section discusses the preliminary obtained multipath models based on the available flight data collected on the
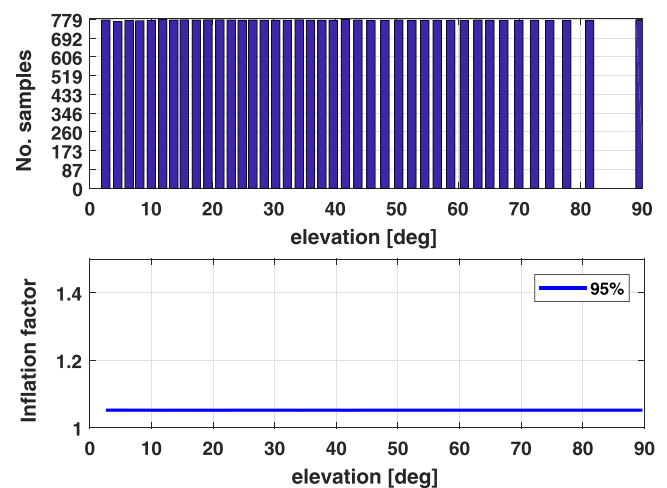

FIGURE 15 Number of independent samples per elevation bin (top plot) and resulting inflation factor to account for limited number of samples (bottom plot) for GPS for fixed 2° elevation bins [Color figure can be viewed at wileyonlinelibrary.com and www.ion.org]

FIGURE 16 Number of independent samples per elevation bin (top plot) and resulting inflation factor to account for limited number of samples (bottom plot) for GPS for bins with equal number of samples [Color figure can be viewed at wileyonlinelibrary.com and www.ion.org]

experimental installation on DLR's A320 (around 200 hours of flight hours). In order to define the multipath models, the following steps are undertaken:

1. Estimation of the smoothed multipath errors using the dual-frequency code-minus-carrier methodology described in Section 2. In this work, the 100-second smoothing time constant is considered. Note again that the smoothed estimates used for deriving the models in this work are selected after the smoothing filter convergence (3.6 times the smoothing time constant).
2. Removal of the code errors introduced by the receiver antenna group delay variations
3. Selection of independent samples (every 350 seconds to account for the correlation of the multipath error; see Figure 14)
4. Overbounding of the data to safely bound the tail risk
5. Inflation in order to account for the limited number of samples
6. Computation of the satellite elevation in the aircraft body frame coordinate system and in the local-level frame (the elevation above the horizon) and comparison of the models obtained in the two local frames

Figures 17 and 18 show the effect of the removal of the code errors due to the antenna group delay variations for GPS and Galileo, respectively. The plots show the
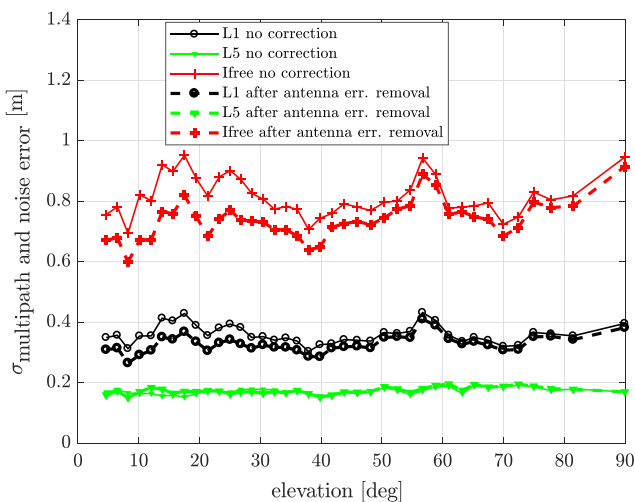

FIGURE 18 Standard deviation of the estimated 100-second smoothed multipath and noise errors from measurements for Galileo E1 (black "o" curves), Galileo E5a ("v" curves), and Ifree (red "+" curves) before antenna error removal (solid lines) and after removal of the code errors introduced by antenna group delay variation (dashed lines) as a function of satellite elevation in aircraft body frame [Color figure can be viewed at wileyonlinelibrary.com and www.ion.org]
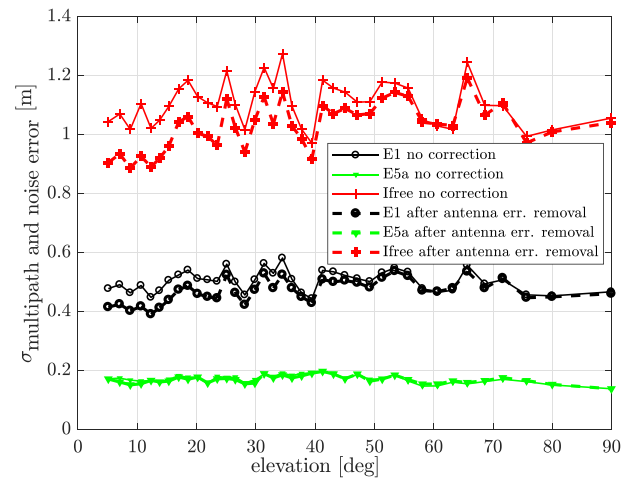
standard deviations of the multipath and noise errors derived from measurements for L1/E1 frequency (in black "o" lines), for L5/E5a frequency (in green "v" lines), and for the Ifree L1/E1-L5/E5a combination (in red "+" lines). The solid lines represent the standard deviation of the multipath and noise error containing also the antenna-induced errors, and the dashed lines show the curves after the code errors due to antenna group delay variations are removed. It can be observed that the removal of the antenna-induced errors has a stronger effect for low-medium elevations (up to 60°). This is because for low elevations, the group delay variation is much larger (see Figure 8). The effect is more pronounced on the L1/E1 band because the antenna performance on the L5 band is better for this antenna and the group delay shows less variation. However, as previously discussed, the effect of the antenna errors is more slowly changing and cannot be quantified only through the standard deviation. It is important to note again that if these errors are not separated, the final derived models might not completely bound the total error present in the pseudoranges due to the multipath estimation process when a part of these errors is removed.

Figure 19 for GPS and Figure 20 for Galileo show the preliminary multipath models obtained after carrying out the steps described previously as a function of the satellite elevation angle in local body frame coordinate system and in local-level frame. The plots show the obtained
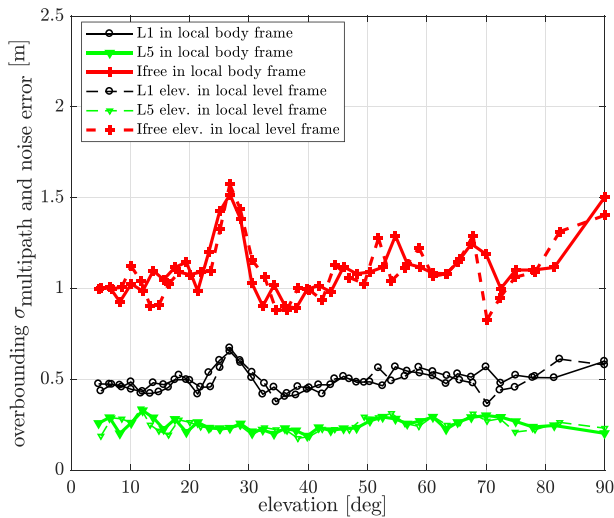

FIGURE 17 Standard deviation of the estimated 100-second smoothed multipath and noise errors from measurements for GPS L1 (black "o" curves), GPS L5 (green "v" curves), and Ifree (red "+" curves) before antenna errors removal (solid lines) and after removal of the code errors introduced by antenna group delay variation (dashed lines) as a function of satellite elevation in aircraft body frame [Color figure can be viewed at wileyonlinelibrary.com and www.ion.org]

FIGURE 19 Overbounding models of the estimated multipath and noise errors from measurements for GPS L1 (black "o" curve), GPS L5 (green "v" curve), and Ifree (red "+" curve) as a function of elevation in A/C body frame (solid lines) and in local level (dashed lines) [Color figure can be viewed at wileyonlinelibrary.com and www.ion.org]
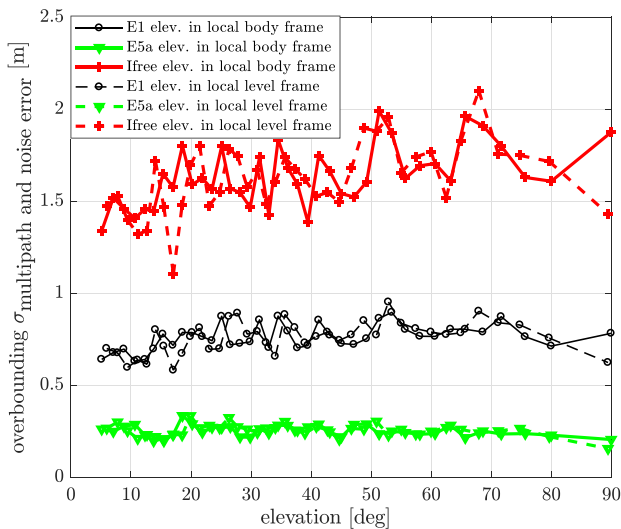

FIGURE 20 Overbounding models of the estimated multipath and noise errors from measurements for Galileo E1 (black "o" curve), Galileo E5a (green "+" curve), and Ifree (red "+" curves) as a function of elevation in A/C body frame (solid lines) and in local-level frame (dashed lines) [Color figure can be viewed at wileyonlinelibrary.com and www.ion.org]

curves for the three models: L1/E1 (with black "o" curves), L5/E5a (with green "v" curves), and L1/E1-L5/E5a Ifree combination (with red "+" curves). The solid lines refer to the models obtained based on the elevation of the satellites in body frame, and the dashed line represents the models obtained when the elevation of the satellite

above the horizon is used (local-level frame). To derive the curves, the elevation bins were selected such that the bins have almost equal number of samples. Note that these models are intended to be preliminary as the equipment used is not compliant with current standards and the main focus of this work is to describe the methodology.

For both constellations, we observe that the differences when considering the two coordinate frames to compute the satellite elevation angles are very small. This effect can be attributed to the smoothing filter with a time constant that is relatively long compared to typical aircraft maneuvers. Thus, based on this experimental data, it can be suggested that the multipath error models can be defined in the local-level frame. This statement needs to be verified when measurements from different airframes and the primary location of the GNSS antenna are available. However, the information of the satellite angle of arrival in a body frame coordinate system is needed and important to be considered for the antenna-induced errors. Future work will investigate how to account for these errors without requiring aircraft attitude information to derive the necessary error bounds for the pseudorange measurements.

Another aspect to notice is that the curves do not show much dependency on the elevation. This effect might be due to our specific installation for which increased multipath is expected for all elevations from different azimuth angles. When the measurements are combined in elevation bins, the multipath spreads over all bins. In addition, the antenna has a poor multipath rejection capability meaning that it will not mitigate the multipath errors from any direction. The lack of elevation dependency will be investigated further in order to confirm it is not specific to this installation.

Comparing the values obtained for GPS and Galileo, the values are slightly different. For L5/E5a, the obtained curves are quite comparable, which is expected as the signal modulation, and the frequency is identical for both signals. For L1/E1, the curves obtained for Galileo E1 are somehow larger than the ones obtained for GPS L1. The reasons might be attributed to the fact that the flight data dates back to 2015, and it cannot be overlooked that variations in the signal quality and signal power level may be reflected in the data. Furthermore, the improved performance of the BOC(1,1) component of the CBOC modulation in multipath rejection is effective on long-range multipath (above 150 m), while on the aircraft, shorter range multipath is present. For short range multipath, the performance of BOC(1,1) modulation is very similar with the one on BPSK(1) modulation.

As already stated, the absolute values obtained for the multipath models are not to be considered final values as

they are derived based on an experimental installation on a single aircraft type. The antenna used in the data collection is noncompliant with dual-frequency antenna MOPS, which leads to worse results than what is expected from a MOPS compliant antenna. Even if the code errors induced by the antenna group delay variations were removed, the antenna multipath rejection capability plays an important role in how much multipath is received. As the antenna used has a small axial ratio, this effect is reflected in the measurements and the obtained results. Furthermore, the antenna was not installed in its primary location but in an experimental location further to the back of the aircraft. In this location, the antenna is closer to other reflectors, and thus, the amount of multipath that is received is higher. Finally, the receiver used was a commercial receiver designed for geodetic applications. While the correlator spacing and the bandwidth were modified to values representative of an avionics receiver, there may be differences in the implementation that need to be investigated.

12 | CONCLUSION

In this work, several aspects for improving the multipath models have been discussed. One of the first issues in estimating the multipath present in the code measurements is that it is affected by integer ambiguities. Typical approaches used to estimate integer ambiguities are to compute the mean over a continuous segment of the satellite or to use the values at the highest elevation as the bias estimation. We showed that these methods are not always suitable to the measurements from flight tests. A new method was proposed that excluded from the integer ambiguity calculation only data that is highly affected by multipath and would lead to a wrong bias estimation.

Secondly, we presented a first concept of separating the antenna-induced errors from the multipath error. The results show that the code errors introduced by the antenna group delay variations have a different signature compared with the multipath error and should not be bounded by a standard deviation only. Future work will investigate the separate bounding of these errors and the impact on performance in terms of availability of protection levels.

Finally, CDF overbounding is proposed for bounding the risk in the tails. This step is especially important for dual-frequency aviation users, where the airframe multipath becomes a dominant source of error. Future work will investigate how to account for bounding probability and integrity exposure interval, along with possible nonzero mean and non-Gaussian multipath distributions with azimuth for a specific elevation bin, particularly if

multipath errors have a maximum size that can be known for an installation or class of installations.

ORCID
Mihaela-Simona Circiu https://orcid.org/0000-0003-4430-0526
Stefano Caizzone https://orcid.org/0000-0002-9434-7368
Michael Felux https://orcid.org/0000-0002-8368-4422

REFERENCES
1. Minimum Operational Performance Standards for GPS Local Area Augmentation System Airborne Equipment. DO-253D, RTCA, 2017.
2. Minimum Operational Performance Standards for Global Positioning System/Satellite-Based Augmentation System Airborne Equipment. DO-229E, RTCA, 2016.
3. Booth J, Murphy T, Clark B, Liu F. Validation of airframe multipath error allocation for local area differential GPS. *Proceedings of the IAIN World Congress and the 56th Annual Meeting of the Institute of Navigation*. San Diego, California; June 2000:689-698.
4. Murphy T, Harris M, Booth J, Geren P, Pankaskie T, et al. Results from the program for the investigation of airborne multipath errors. *Proceedings of the 2005 National Technical Meeting of the Institute of Navigation (NTM 2005)*. San Diego, California; January 2005:153-169.
5. Murphy T, Harris M, Booth J, Geren P, Pankaskie T, et al. More results from the investigation of airborne multipath errors. *Proceedings of the 18th International Technical Meeting of the Satellite Division of the Institute of Navigation (ION GNSS 2005)*. Long Beach, California; September 2005:2670-2687.
6. Caizzone S, Circiu MS, Elmarissi W, Enneking C, Felux M, et al. Effect of antenna pattern uniformity on the pseudorange tracking error. In *Proceedings of the 30th International Technical Meeting of the Satellite Division of the Institute of Navigation (ION GNSS+ 2017)*. Portland, Oregon; September 2017:3460-3470.
7. Caizzone S, Circiu MS, Elmarissi W, Enneking C, Felux M, Yinusa K. Antenna influence on Global Navigation Satellite System pseudorange performance for future aeronautics multi-frequency standardization. *NAVIGATION*. 2019;66:99-116. https://doi.org/10.1002/navi.281
8. Hatch R. The synergism of GPS code and carrier measurements. In *Proceedings of the 3rd International Geodetic Symposium on Satellite Doppler Positioning DMA/NOS*. Washington D.C.; 1982:1213–1231.

9. Murphy T, Snow R, Braasch M. GPS multipath on large commercial air transport airframe. *NAVIGATION*. 1996-97;43:397-406. https://doi.org/10.1002/j.2161-4296.1996.tb01928.x

10. Harris M, Miltner M, Murphy T, Raghuvanshi A, van Graas F. Bounding GPS L1 antenna group delay variation for GNSS landing system integrity. *Proceedings of the 2017 International Technical Meeting of the Institute of Navigation*. Monterey, California; January 2017:591-605.

11. ED-259. *Minimum Operational Performance Standard for Galileo/Global Positioning System/Satellite-Based Augmentation System Airborne Equipment*. Version 0.9; December 2018.

12. DO-373. *Minimum Operational Performance Standards for GNSS Airborne Active Antenna Equipment for the L1/E1 and L5/E5a Frequency Bands*. RTCA; 2018.

13. Eurocae ED-114A. *Minimum Operational Performance Specification for Global Navigation Satellite Ground Based Augmentation System Ground Equipment to Support Category I Operations*. March 2013.

14. Kaplan E, Hegarty C. *Understanding GPS. Principles and Application*. Second ed. ; 2006 ISBN: 1-58053-894-0.

15. IS-GPS200D. *Navstart GPS Space Segment/Navigation User Interfaces*. December 2004.

16. Thoelert S, Vergara M, Sgammini M, Enneking C, Antreich F, et al. Characterization of nominal signal distortions and impact on receiver performance for GPS (IIF) L5 and Galileo (IOV) E1/E5a signals. *Proceedings of the 27th International Technical Meeting of the Satellite Division of the Institute of Navigation (ION GNSS+ 2014)*. Tampa, Florida; September 2014:3113-3128.

17. Wanninger L, Sumaya H, Beer S. Group delay variations of GPS transmitting and receiving antennas. *Journal of Geodesy*. 2017;9:1099-1116.

18. Vergara M, Sgammini M, Thoelert S, Enneking C, Zhu Y, Antreich F. Tracking error modeling in presence of satellite imperfections. *NAVIGATION*. 2004;63:3-13. https://doi.org/10.1002/navi.129